AERODYNAMIC ANALYSIS OF ROTOR/PROPELLER WAKES INTERACTIONS ON HIGH SPEED COMPOUND HELICOPTER

Ronan Boisard, ronan.boisard@onera.fr, ONERA (France)
Joon W. Lim, w.lim.civ@mail.mil, U.S. Army (USA)

Abstract
In the context of the development of high speed compound helicopters, the main rotor may not be an efficient propulsive device at high speeds and a propeller has to be added in order to reach high advancing velocities. On such configuration, at low speed, the propellers are in strong interactions with the main rotor wake which affects their performance and aircraft maneuverability. The present work numerically investigates the aerodynamics of the rotor / propeller interaction on rotorcraft similar to the Racer from Airbus Helicopters. Through the comparison of two different levels of modeling it is shown that at high advance ratio, a simple free wake model is suitable to give most of the interaction effects, while in hover, a full CFD unsteady computation is necessary to precisely capture all the unsteadiness of the interaction. By comparing two different CFD solvers it also demonstrates that the results are highly sensitive to the choosen numerical setup. This paper also outlines the different behaviors of the propeller when it is fully inside the rotor wake or out of it, and therefore the need for a precise control of the rotorcraft in the transition between hover to fast forward flight.

1. NOTATION

c	Blade chord, m
R	Rotor radius, m
r/R	Non dimensional spanwise location
Vo	Freestream velocity, m/s
V_{tip}	Blade tip rotation velocity, m/s
μ	Advance ratio, $\frac{V_o}{V_{tip}}$
Ω	Rotational velocity, rad/s
b	Number of blades
σ	Rotor solidity, $\sigma = \frac{b\,c}{\pi\,R}$
ρ	Air density, kg/m^3
a	Speed of sound, m/s
S	Rotor disk surface, m²
F_X	Axial force, N
X_{bar}	Axial force coefficient, $\bar{X} = \frac{100\,F_X}{1/2\ \rho\,S\,\sigma\,(R\,\Omega)^2}$
F_z	Thrust, N
Z_{bar}	Thrust coefficient, $\bar{Z} = \frac{100\,F_Z}{1/2\ \rho\,S\,\sigma\,(R\,\Omega)^2}$
C_nM^2	Section normal force coefficient $C_nM^2 = \frac{F_n}{\frac{1}{2}\rho a^2 c}$
C_cM^2	Section chordwise force coefficient $C_cM^2 = \frac{F_c}{\frac{1}{2}\rho a^2 c}$
RMS	Root Mean Square: $RMS = \sqrt{\overline{X^2} - \bar{X}^2}$
θ_0	Blade collective pitch angle (positive up)
θ_{1c}	Blade lateral cyclic pitch angle
θ_{1s}	Blade longitudinal cyclic pitch angle
β_0	Blade coning angle (positive down)
β_{1c}	Blade longitudinal cyclic flap angle
β_{1s}	Blade lateral cyclic flap angle
δ_0	Blade lead-lag angle (positive lead)
δ_{1c}	Blade longitudinal cyclic lead-lag angle
δ_{1s}	Blade lateral cyclic lead-lag angle

2. INTRODUCTION

Helicopters have typically more than one rotor. While a conventional helicopter has a main rotor and a tail rotor, tandem, coaxial, and tiltrotor aircraft have multi-rotors to ensure both lifting and propulsive forces. In the context of the development of high speed compound helicopters, the main rotor may not be an efficient propulsive device at high speed and a propeller has to be added in order to reach high advancing velocities. Multiple rotors are also commonly found in the field of UAVs, where the lifting function is often distributed on several rotors. The simultaneous use of rotating blades distributed around the airframe with planes of rotations that may differ (Figure 1) adds a lot of aeromechanical complexity and can lead to complex unsteady interactions between the wakes emitted from the different rotors and propellers. It is legitimate to assume that such interactions, of aerodynamic nature, can have a significant impact on vibrations, radiated noise and aerodynamic performance, especially in low speed conditions.
Aerodynamic interactions between rotor and fixed airframe surfaces have been studied for a long time. Main rotor / fuselage interactions are now well understood and can be predicted thanks to numerical tools which were validated against experimental results [1], [2]. Main rotor/tail rotor interactions are also well documented, they were for example the main focus of the European project GoAhead involving several European organizations [3]. However it is difficult to find studies on rotor / propeller wake interactions at low speeds. Literatures available on the subject typically contain a very limited scope. For example, US Army carried out an experimental study simulating co-axial and tandem configurations [4] which was limited to hover cases. It seems that little attention has been

Presented at 47th European Rotorcraft Forum, United Kingdom, 7-9th September, 2021

paid to rotor/propeller wake aerodynamic interactions. The extensive study of compound helicopter with side propellers was performed back in the sixties [5]. The study was also limited to relatively high advance ratio for which wakes interactions were minimal, mainly focusing on vibratory loads with a full aircraft (main rotor, fuselage, wing and propeller). More recently some small scale experiment was conducted by Sikorsky and UTRC on a configuration similar to the X2 and the Raider [6] but once again, only the effect on the full rotorcraft was of interest.

Figure 1: Sikorsky S-97 Raider (left), Airbus Helicopter RACER (right)

The objective of this paper is to investigate the aerodynamics of rotor/propeller wake interactions on a rotorcraft similar to the X3 or the Racer demonstrators of Airbus Helicopters. This study will provide some insight on the effects of the propeller and main rotor interactions and also provide the results necessary to judge whether simple approaches like lifting line methods are sufficient to capture the phenomena or a full URANS (Unsteady Reynolds-Averaged Navier-Stokes Simulation) CFD computation is mandatory. Some work on the same rotor / propeller setup was already published in 2018 [7], however, the present work is an improvement of the URANS CFD computations from then and also includes comparisons with another CFD solver.

3. INTERACTIONAL SETUP

Since a couple of years, ONERA has investigated the rotor/propeller wake interactions and built an experimental test rig dedicated to this topic (Figure 2).

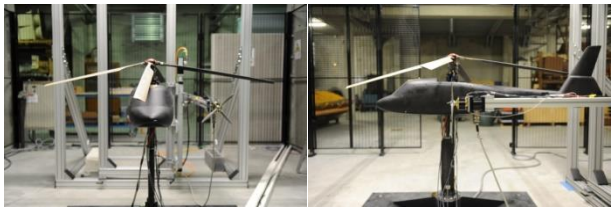

Figure 2: ONERA test rig for Rotor / Propeller wake interaction study

The main rotor is based on a Dauphin helicopter test rig which was already extensively used to study rotor / fuselage interactions more than a decade ago [8]. The propeller part is based on an off-the-shelve propeller designed for remotely controlled aircraft by APC Propellers 9.

All the work shown here is based on this experimental setup as the computations are pre-test ones intended to be used to size the test rig and decide what are the most interesting points for measurements. The thrust and power of the propeller and main rotor will be measured using balances, and some PIV measurements are also planned in order to have a closer view of the wake interactions. Unfortunately there are no pressure taps in the blades. The isolated propeller was tested in the low speed L2 ONERA wind tunnel in Lille March 2021 and the full setup is scheduled to be tested by summer 2021.

3.1. The main rotor

The helicopter model is a 1/7.7 scale Dauphin 365N model equipped with a 4 bladed fully articulated main rotor of 1.5m diameter. In the experiment the rotor trim will be obtained by the adjustment of collective and cyclic pitch angles by means of swashplate actuators. The rotor shaft is tilted 4° forward (nose down). The blades are rectangular with a constant OA209 airfoil, a chord of 0.05m and a linear twist of -12°/R. The rotor is not Mach-scaled. It rotates clockwise at 1272 RPM and its tip speed is 100m/s. But this is not an issue since the main goal here is to study wake interactions at low advance ratios where compressible effects are not so important.

3.2. The side propeller

The propeller was chosen in order to be consistent in terms of diameter, thrust and tip speed with the main rotor compared to an actual rotorcraft of this type. It is a four bladed, fixed pitch, puller propeller of 28cm diameter made by APC Propellers [9]. Details of the blade geometry were kindly provided by the manufacturer. The rotation speed of the propeller was set to 1/6 of the main rotor RPM in order to be able to have a periodic setup in the computations to ease the postprocessing and analysis of the results.
In experiment the propeller can be added and moved around the fuselage at any position. However, for the pre-test computations, only one position of the propeller relative to the rotor was investigated. The propeller was set 0.14m (0.187R MR) ahead of the rotor center, on the rotor advancing side (0.375m from the rotor center, i.e. 0.5R MR) and 0.28m (0.373R MR) below the rotor head. This positioning is approximately what was used on the X3 helicopter from Airbus Helicopters.

3.3. Flight conditions

A target value of Z_bar=14.5 was chosen for the main rotor. This corresponds to a medium thrust condition for which wake interactions are expected to be relatively important. In the experiment, the rotor trim will be performed so that net axial force acting on the model will be zero (X_bar=0.), and the lateral flapping angle will be zero (β_1s=0.). For that

purpose, the trim values of the rotor pitch, flap and lead-lag angles, are obtained from a comprehensive analysis code in terms of harmonics (Table 1) and used throughout all the computations. Note that the trim conditions were obtained for each advance ratio on an isolated rotor and used also for the installed configurations.

Concerning the advance ratio, several different operating conditions were investigated. Figure 3 shows a simple sketch of the expected rotor wake deflection in a plane passing through the propeller center for different advance ratios. In the hovering condition (μ=0.00) the propeller is fully immersed in the rotor wake. At an advance ratio of 0.05, the propeller is partially in the rotor wake and the rotor / propeller wake interactions remain extremely important. At a 0.10 advance ratio, the propeller itself is no longer in the rotor wake but it remains very close, and above an advance ratio of 0.15, both wakes are only slightly interacting. In the computations, only advance ratios from 0.0 to 0.25 were investigated. Moreover, an advance ratio of 0.20 correspond to the maximum wind speed of the wind tunnel that will be used for experiments.

μ		0.00	0.05	0.10	0.15	0.20
Shaft Angle		-4°	-4°	-4°	-4°	-4°
Pitch	θ_0	9.9°	9.6°	8.19°	7.34°	7.10°
	θ_{1c}	-0.21°	1.20°	2.15°	2.17°	2.14°
	θ_{1s}	3.77°	2.70°	2.12°	1.64°	0.99°
Flap	β_0	-2.93°	-3.04°	-2.86°	-2.76°	-2.75°
	β_{1c}	3.95°	3.68°	3.69°	3.74°	3.70°
	β_{1s}	0.00°	0.00°	0.00°	0.00°	0.00°
Lead-Lag	δ_0	-4.85°	-4.56°	-3.29°	-2.60°	-2.33°
	δ_{1c}	-0.05°	0.03°	0.09°	0.10°	0.10°
	δ_{1s}	-0.21°	-0.21°	-0.19°	-0.18°	-0.17°

Table 1: Rotor trim as a function of advance ratio.

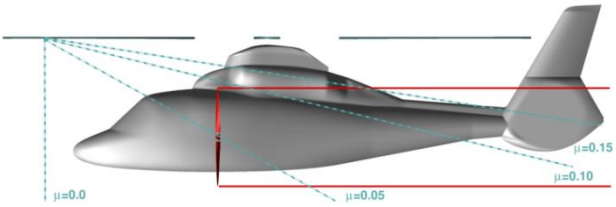

Figure 3: Sketch of isolated propeller and rotor wake path at different advance ratio

4. NUMERICAL METHODS

In this study, two different numerical methodologies are used. The first one is a fast response method based on a lifting line approach coupled with an unsteady free wake model. The second one is much more computationally expensive and relies on URANS CFD using two different solvers: elsA from ONERA and HPCMP CREATETM-AV Helios from US Army.

4.1. Unsteady free wake method

Free wake computations are based on the PUMA (Potential Unsteady Methods for Aerodynamics) code, which has been developed at ONERA since 2013. It is built on a coupling between an aerodynamic module and a kinematic module. The aerodynamic module relies on lifting line method with a free wake model. The free wake model is based on Mudry theory [10] which rigorously describes the unsteady evolution of a wake modelled by a potential discontinuity surface. The lifting line method relies on 2D airfoils characteristics. It can handle some 3D corrections for blade sweep and 2D unsteady non linear aerodynamics effects through dynamic stall models. Moreover, different time discretizations are available in order to balance between accuracy, numerical stability and computational time. At last, influence of any arbitrary surface onto the wake can be taken into account using a potential approach. Concerning the kinematic module, it is based on a rigid multi-body system approach using a tree-like structure with links and articulations. In order to speed up the computation the code has been parallelized using OpenMP and the Multilevel Fast Multipole Method has been implemented for the computation of the velocities induced by each wake panel on any element. PUMA is used at ONERA for any aerodynamic study of fixed wings and rotating wings configurations which requires low computational cost or a large amount of parametric investigations like pre-design studies. It has also recently been successfully applied for helicopter rotors wake in interactions with obstacles as discussed in [11] and [12].

The airfoil data needed for the PUMA computations were computed using elsA CFD solver [13] for a constant Reynolds number over Mach number corresponding to the rotor scale. Concerning the numerical parameters used for the computations, they are based on ONERA previous experience on the use of PUMA for helicopter rotors and propellers and parametric study. The most meaningful parameters are:

- ✓ 12 radial stations for blade definition.
- ✓ 25 radial stations for wake emission using square root distribution along the span.
- ✓ 2° time steps for the rotor (12° for the propeller).
- ✓ No modelling of the helicopter fuselage and test rig.

Depending on the advance ratio, between 5 to 15 wake revolutions were kept in order to compute the induced velocities and between 15 to 40 rotor revolutions were computed to ensure acceptable convergence, with an averaging of the loads over the last 5 main rotor revolutions. Note that even if a lot of rotor revolutions were computed, unsteadiness is quite important and no significant

periodicity can be reached at low advance ratio. Moreover, for the hover case, numerical parameters have to be tuned in order to stabilize the computation and the way the numerical parameters are tuned can highly affect the solution.
Free wake methods are relatively fast responding methods. However, due to the difference in terms of rotational speed between the propeller and the rotor, the required computational time is still large.

4.2. *elsA* CFD solver

The first batch of URANS CFD computations are performed using the ONERA elsA software [13]. The computations are based on structured grids with overset approach.
The rotor and propeller blades grid are built using Pointwise® software. The rotor blade surface grid counts 151 points in the chordwise direction per blade side and 231 points in the spanwise direction. The propeller blade surface grid counts 159 points in the chordwise direction per blade side and 171 points in the spanwise direction. Extension of the grids around the blade is approximately 0.5 to 1.0 blade chord for a total number of mesh points of roughly 3.9 million per propeller blade and 5.8 million for each rotor blade. To be fully consistent with the free wake computations, the fuselage was not taken into account.

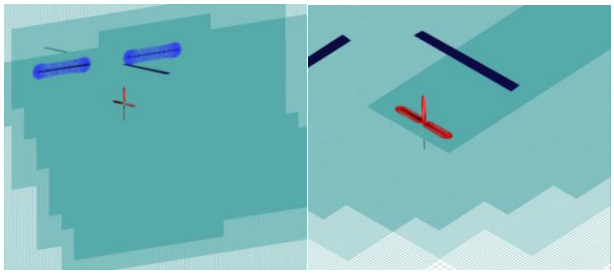

Figure 4: Iso Y (left) and Iso Z (right) view of the CFD mesh for interactional computation at μ=0.05

The background mesh is a Cartesian grid automatically generated using Octree approach. The full grid counts 9 grid levels with a one over two cell size increase between each level. The background grid extends up to roughly 10 rotor diameters in the farfield. The mesh is refined in the vicinity of the blades up to a level of approximately 9% of the blade chord. A view of the mesh for advance ratio 0.10 is given in Figure 4. Depending on the test cases, the final meshes count from 300 million points to 440 million points.
Computational parameters used are based on ONERA best practices on such kind of configurations. The time scheme used is a 2nd order implicit backward finite difference scheme solved by a Newton algorithm. In order to ensure good accuracy the number of Newton sub-iterations was set to 25 and a physical time step corresponding to an azimuthal angle of 0.1° on the main rotor was used throughout the whole computations. Due to the low velocities involved in these computations, a version of the 2nd order AUSM+P scheme adapted to low Mach number flow 14 was used. K-ω Kok [15] model was used for the turbulence with Zheng limiter and SST correction. Computations were performed in the absolute velocity formulation using an absolute reference frame.
While for the isolated rotor and propeller computation, the convergence criteria is easy to define (no significant variations of mean thrust between two revolutions) and can be reached in relatively few rotor revolutions, it is much more difficult for the interactional setup. The hover case even seems to never reach a periodic state due to the strong interactions involved. In hover, 15 rotor revolutions were computed, 9 for other advance ratio values and the loads were averaged over the last one, even if it may not be fully sufficient for the hover case.

4.3. *HELIOS* CFD solver

The second batch of URANS CFD computations are performed using the HELIOS software [16] which is also based on the structured grid with an overset approach.
The HPCMP CREATE™-AV Helios code is a high-fidelity, multidisciplinary rotorcraft modeling software developed under the sponsorship from High Performance Computing Modernization Program Computational Research and Engineering Acquisition Tools and Environments – Air Vehicles program and the US Army. The basic CFD meshing approach in Helios is to use a multi-mesh paradigm – near-body body-fitted curvilinear or unstructured meshes are used to model rotor components such as blades, hub, fuselage etc., and an off-body Cartesian mesh is used to model the background regions (wakes) away from these components. These meshes form an overset mesh system, and a domain connectivity module is used to manage the overset mesh communication among them.

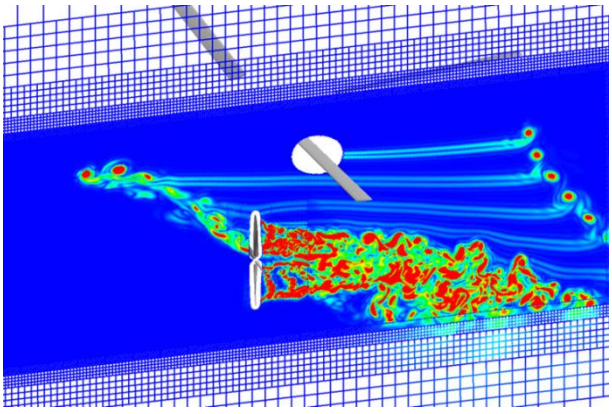

Figure 5: Helios volume mesh longitudinal cutoff plane passing the propeller hub center displaying Q iso-surfaces for the interactional computation at μ=0.05.

The rotor blade surface grids count 117 points in the chordwise direction per blade side and 111 points in the spanwise direction. The propeller blade surface

grids count 101 points in the chordwise direction per blade side and 64 points in the spanwise direction. Extension of the grids around the blade is approximately 1.2 blade chords, resulting in a total number of mesh points of roughly 1.57 million per propeller blade and 2.58 million for each rotor blade. It is noted that the mesh points include the blade itself and the blade root and cap grids.
The background mesh is structured Cartesian grids and the full grids comprise 9 grid levels. The background grids extend up to roughly 10 rotor radii in the farfield. The background mesh in the vicinity of the propeller blades is refined up to a level of approximately 5% of the propeller blade chord by introducing a fixed refinement mesh. A cut-through view of the Helios volume meshes at an advance ratio of 0.05 is given in Figure 5. The total background mesh points are 447 million points with fringes and 284 million points without fringes.

	elsA	Helios
Near-body solver	elsA	OVERFLOW
Rotor nodes	23.2 M	10.4 M
Rotor blade mesh	151 x 231 x 75	117 x 111 x 77
Prop nodes	15.6 M	6.3 M
Prop blade mesh	151 x 171 x 66	101 x 64 x 77
Spatial scheme	2nd order	5th order
Temporal scheme	Dual time step 25 subiterations	Dual time step 30 subiterations
Turbulence model	k- ω SST	k- ω SST
Off-body solver	elsA	SAMCART
Off-body nodes	275M – 460M	284M (no fringes)
Finest mesh space	9% prop chord	5% prop chord
Spatial scheme	2nd order	5th order
Temporal scheme	Dual time step 25 subiterations	2nd order implicit 15 subiterations

Table 2: Comparison of elsA and Helios CFD tools.

The elsA and Helios codes are compared in Table 2. Although the HELIOS and elsA mesh count almost the same number of points, the finest grid spacing in elsA is coarser than in HELIOS but it extends over a larger area.
The time step sizes in time integration were set to the same value as in elsA i.e. 0.1° for the rotor and 0.6° for the propeller, which reflects a RPM ratio of 1 to 6 between the rotor and propeller. Strong rotor/prop interactions were expected for hover and advance ratio 0.05. To achieve convergences, the computation was made over 14 rotor revolutions for hover and 10 rotor revolutions for μ = 0.05 whereas the computations were made only for 5 rotor revolutions at higher speeds.

4.4. Postprocessing convention

In the following sections, the thrust and power will be defined as forces and moments with respect to the vertical axis for the rotor and the horizontal axis for the propeller. In plane forces and moment, along with azimuthal blade positions will be defined with the convention given in Figure 6.
When considering installation effects, the different values are obtained on the basis of:

$$InstallationEffect = \frac{(InstalledValue - IsolatedValue)}{IsolatedValue} \times 100$$

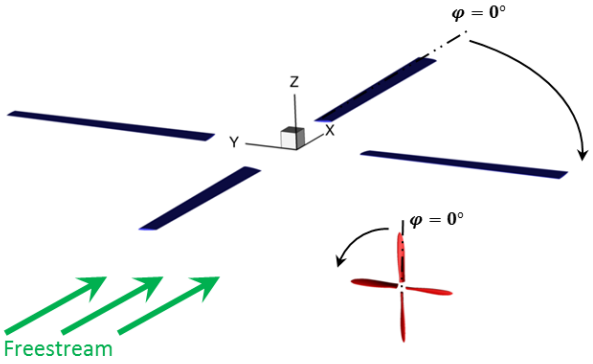

Figure 6: Rotor and propeller convention axis and orientation.

5. NUMERICAL RESULTS

Figure 7 summarizes the interactional effect on the rotor and propeller performance as a function of advance ratio. For both rotor and propeller, the variations of thrust and torque are expressed in percent of the nominal value obtained in isolated conditions. It clearly outlines the three different interactional conditions already foreseen in Figure 4:

- ✓ Hover case: The propeller is fully immersed in the rotor wake, with no freestream velocity to push the rotor and propeller wake backward from the helicopter. It seems to induce large changes in torque and thrust on the propeller and only small effects on the main rotor. However there is some large scattering between the different simulations.
- ✓ Low advance ratio case, μ=0.05: The propeller is partially immersed in the rotor wake, but both wakes are pushed away from the rotor due to the free stream velocity. This condition is somewhat a transitional condition between hover and forward flight. The effect on the main rotor seems larger than in the hover case and the propeller is affected in a very different way. But once again some large scattering is observed between the different numerical approaches.
- ✓ Advance ratio higher than 0.10: The rotor wake does not directly interact with the propeller blades and minor wake interactions are seen. It seems to induce a very small increase in propeller thrust with almost no change in the propeller power along with small effects on the main rotor. For these conditions all the numerical tools agree very well.

The hover and low advance ratio cases one feature very strong interactions and seems to be difficult to predict. Moreover it is extremely important for

aircraft stability to perfectly understand the physics of the transition phase between hover and the forward flight. Therefore they will be investigated in more details in the following sections. For higher advance ratio, all numerical tools seem to agree with each other, and the physics of the interaction is also simpler. It was already analyzed in details in 7 therefore the present paper will not focus on these low speed flight conditions.

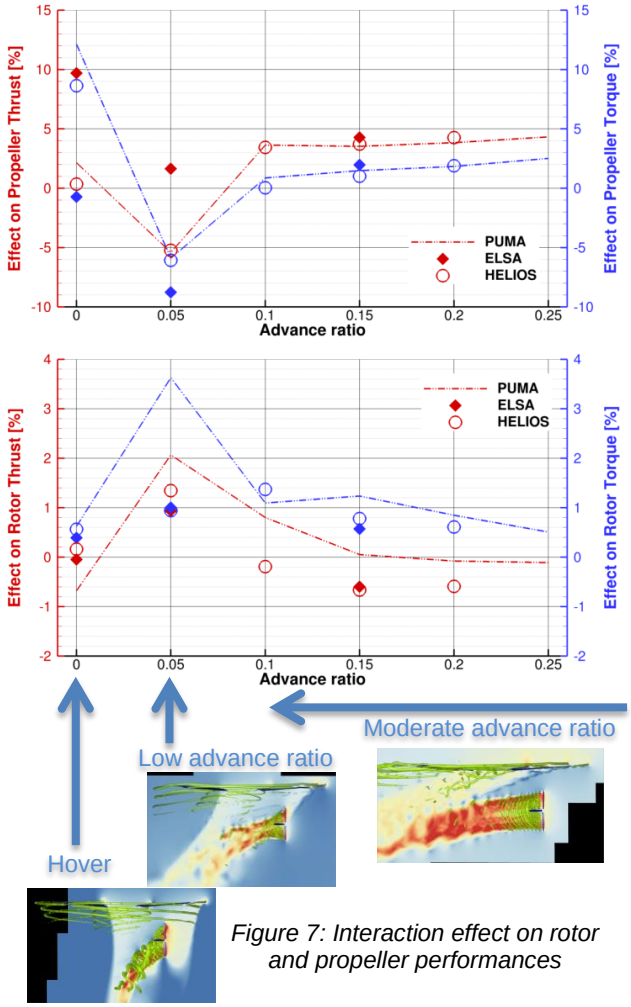

Figure 7: Interaction effect on rotor and propeller performances

5.1. Hover conditions (Mu=0.00)

As shown in Figure 8 in hover, the propeller is fully immersed in the main rotor wake which seems to be sucked into the propeller. The propeller wake is also rapidly pushed downward.

In such extreme conditions, it must be said that the free wake approach suffers from important instabilities. The intersections between lifting line and wake panels introduce larges discontinuities in the induced velocities computations and some regularization parameters have to be introduced. The tuning of such numerical parameters in order to avoid divergence could largely affect the results. Moreover, the number of revolutions computed had to be reduced. The choice of these numerical parameters can impact the results

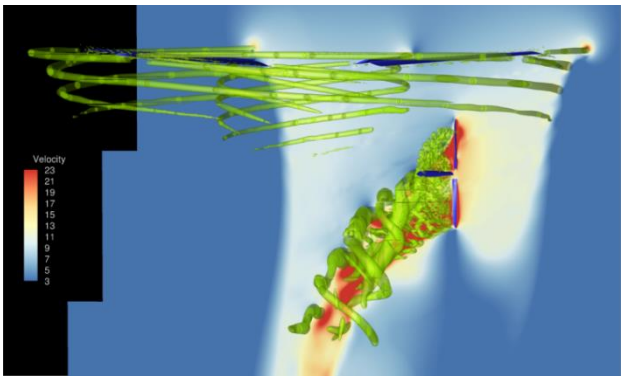

Figure 8: Velocity in a plane perpendicular to the propeller disc in hover conditions (elsA)

5.1.1. Effect on the main rotor

Table 3 illustrates installation effects on the main rotor thrust and power for the different numerical tools. Concerning the power, all tools are expecting a small increase. But for the thrust, while elsA and PUMA are predicting a small decrease, Helios is featuring a small increase. However, the largest values are of the order of 0.5% and discrepancies between CFD codes are of the order of 0.1%. So we can conclude to a relatively good agreement between all the codes with almost not effects on the averaged main rotor loads.

	Thrust[1] [%]	Power[1] [%]
PUMA	-0.68%	0.63%
elsA	-0.05%	0.39%
Helios	0.16%	0.56%

[1]Time average over one rotor revolution (six propeller revolutions)

Table 3: Installation effect on main rotor thrust and power in hover

Although, no effect is observed on the time averaged loads, it does not mean that the propeller does not interact with the main rotor. Figure 9 shows the installation effect on the contribution to thrust and power of one rotor blade along a full revolution. As a matter of fact, all numerical tools show some non-negligible effects on the advancing side in the propeller vicinity, around 90° of azimuth. PUMA computation also shows some important effect on the retreating side. It seems that this effect on the retreating side is mainly numerical and only due to a lack of convergence due to the necessity of tuning the numerical parameters to avoid divergence. Moreover, there is a large increase of power with a small decrease of thrust, which could be interpreted as stall behaviors. This issue is often encountered in transient flow due to important circulation on wake panels in such computations leading to unphysical stall but should disappear when convergence is reached. Such large effects were seen on the CFD computation before it fully reached convergence with sufficient rotor revolution computations. At the end, the CFD computations only shows very small effects on the retreating side.

This effect is due to the deviation of the main rotor wake and also the blade root vortices due to the propeller wake.

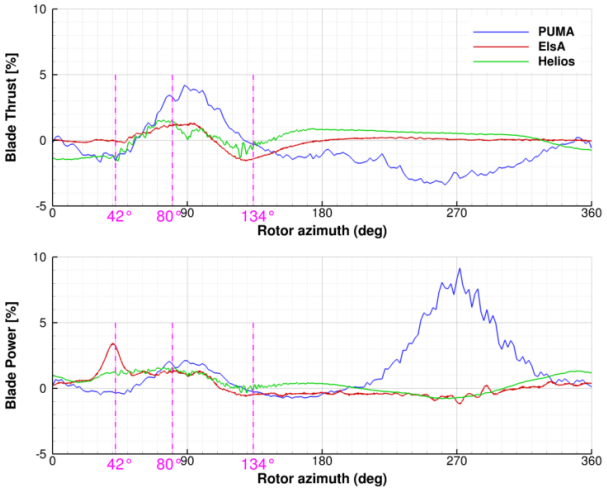

Figure 9: Installation effect on one main rotor blade thrust and power in hover

The effects on the advancing side are more interesting. All the computations agree on an increase of thrust and power for the rotor blade between 55° to 105°. This increase of thrust is due to the propeller to rotor wake effect. The propeller near wake is relatively close to the main rotor and its induced velocities are locally increasing the main rotor blade sectional angle of attack leading to this increase of thrust and power. Both CFD codes give a similar increase in this area.

Between 105° and 180°, the installation effect produces a loss of thrust in both CFD computations. In this area, the main rotor blade is in front of the propeller. The propeller is accelerating the flowfield producing some suction through the main rotor disc contributing to a decrease of the blade sectional angle of attack thus reducing the loads.

Between 0° and 70° elsA and Helios are showing more discrepancies. On the thrust Helios is predicting a larger loss than elsA and on the power, elsA is featuring an important bump at 42° which is not seen by Helios. At those azimuths, the main rotor blade is above the propeller far wake, some dissipation has already occurred and the wake is pushed downward by the main rotor downwash. While the bump on the power found no physical explanation, the small loss of thrust could be due to the propeller wake axial velocity that combines with the main rotor downwash leading to an acceleration of the flowfield in this area, and therefore a loss of thrust. The curvature of the propeller wake is clearly visible on Figure 8 and seems to cause an acceleration of the main rotor wake.

The reduction of loads in front of the propeller position and the increase above the propeller near wake strongly depends on the propeller thrust which in turns is a function of how much the main rotor wake is disturbing the propeller. There is a strong coupling between the two elements and the result is highly dependent on the numerics of the computations which leads to different wake strength, wake dissipations, … Considering that the results are coming from two different codes with very different numerics, the CFD results are actually in quite good agreement.

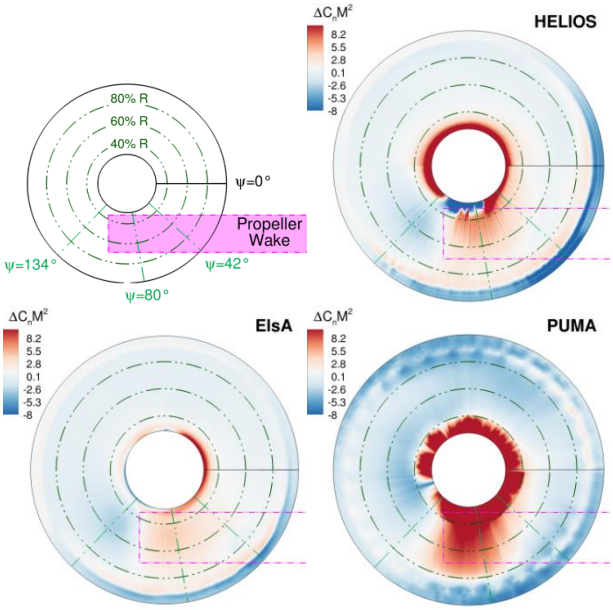

Figure 10: Change in main rotor sectional load due to interactions in hover

Figure 10 shows the interaction effect on the main rotor sectional loads over one revolution. Most of the features that were foreseen from the blade spanwise integrated loads are confirmed here. All the computation feature a red spot (increase of loads) behind the propeller plane followed by a blue spot (decrease of loads) in front of the propeller. Some effects are also visible near the blade root and tip, those are due to a change of tip and root vortex strength due to the change in the blade loading. Spanwise load distribution at three different blade azimuths is compared in Figure 11. In front of the propeller, at 134° azimuth, elsA and Helios give very close results, except at the very tip and root of the blade meaning that differences relie mainly on how the solver captures the effect of the interactions on tip and root vortices. More over at blade root, loads is very close to zero, therefore small differences between installed and isolated computations lead to very large percentage of change. Most of the blade encounters the propeller suction effect, leading to a decrease of loads. PUMA computation also features similar results, loads gradients are only slightly smaller and may suffer from a much coarser spanwise distribution of blade sections modeled.

Above the propeller near wake, at 80° azimuth both CFD results are also very close for blade sections that are not above the propeller wake (above 70% radius). For lower radius, discrepancies are increasing and may be linked to the small

differences in propeller thrust and therefore suction effect on the main rotor wake. Concerning PUMA computations, there is a loss of loads near the blade tip and a large overestimation of the increase of loads for radial stations below 80%.

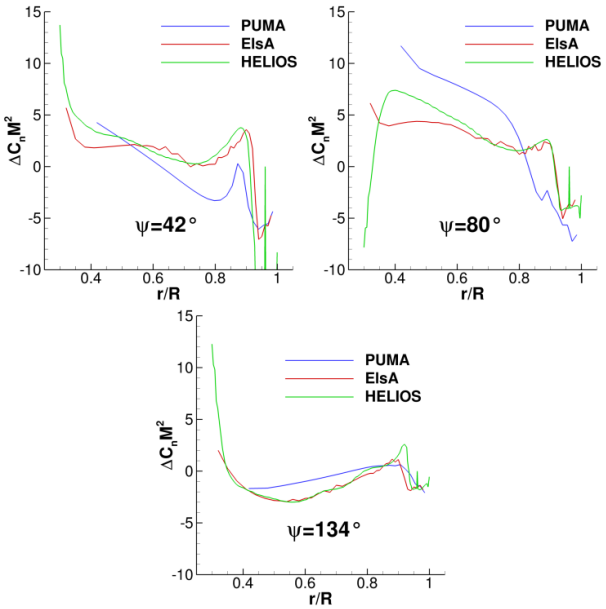

Figure 11: Change in main rotor sectional load radial distribution due to interactions in hover

As shown in Figure 11, at 42° azimuth, where the spanwise integrated loads are featuring a bump on the elsA computation (Figure 9), both CFD results are actually very close. The main differences are in the large increase of loads near the root and the extreme loss near the tip predicted by Helios while elsA only sees a moderate increase and loss. Thanks to higher order scheme, Helios may produce stronger root and tip vortices whose path may be different between isolated and installed case due to the propeller. As it was the case for the azimuth above the propeller near wake, PUMA behavior is very different from the CFD computations. It clearly shows that lifting line approach, due to convergence issues, is not, in its current implementation, suitable to predict local flowfield behavior on the main rotor.

While there was almost no effect on the time average rotor loads, it was shown that locally the loads are largely affected by the propeller wakes. It should be reminded that all the computations were performed using isolated rotor trim. But in real case, the trim, at least flap and lead-lag angles, may be affected by these interactions.

5.1.2. Propeller inflow characteristics

In order to better understand the effect of the main rotor on the propeller, it is interesting to first have a look at the propeller inflow. To do so, Figure 12 shows the three velocity component in the propeller plane from a computation of an isolated rotor.

In hover there is no freestream velocity and the propeller disc is fully inside the rotor wake. We can first note that all the velocity components are relatively homogeneous over the full propeller disc, with almost not fluctuations (RMS below 1m.s^{-1}). Both axial (Vx) and lateral (Vy) velocities are mainly driven by the main rotor wake swirl and contraction, and remain very low: below 1m.s^{-1} for the axial one and of the order of 2m.s^{-1} for the lateral one. However the vertical velocity (Vz) which is due to the main rotor downwash is quite large, above 10m.s^{-1}. On all the components, some small changes in the velocities are seen on left side of the disc (propeller blade down) which is actually below the inner part of the main rotor blade. Those changes are due to the main rotor blade root vortices interactions.

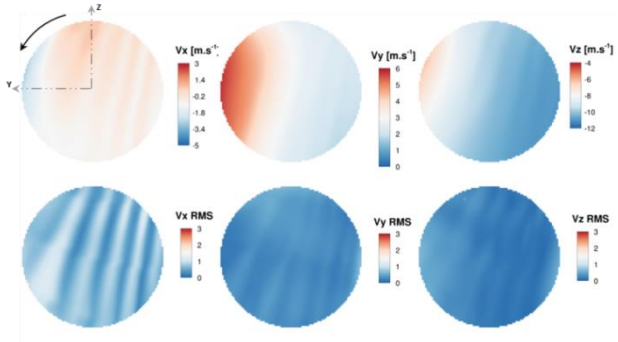

Figure 12: Velocity (mean value and RMS) in propeller plane from an isolated rotor computation (elsA) in hover

From these observations, it can be anticipated that the propeller will be mainly affected by the main rotor downwash and we could expect large increase of loads on the blade up side, and large decrease on the blade down side.

5.1.3. Effect on the propeller

Table 4 illustrates the installation effects on the time average propeller thrust and power for the different numerical tools over one rotor revolution (six propeller revolution). It also include the time average lateral (Fy) and vertical (Fz) forces (respectively moments) acting on the propeller in installed conditions as a percent of the thrust (respectively power). In isolated conditions these in plane forces and moments are strictly equal to zero. On the thrust and power there is an important scattering between the different tools. Helios only predicts a very small increase of thrust along with a large increase of power, while elsA is predicting an important increase of thrust with only minor changes on the power. PUMA follows the same trends as Helios but with some overestimation on the increase of thrust and power. Concerning the in-plane forces and moments all tools give the same trends. An important vertical force along with a small lateral one which is quite similar to what is observed for a propeller under angle of attack. Concerning the moments, all tools also agree, and the most critical values are maybe the yawing moment which reaches more than 70% of the torque. Once again it

is typical from a propeller with angle of attack and due to the dissymmetry of loads between the blade moving up and the one moving down.

	PUMA	*elsA*	HELIOS
Thrust change[1]	2.14 %	9.70%	0.35%
Fy[1,2]	-1.58%	-0.08%	-1.11%
Fz[1,2]	-8.16%	-5.94%	-6.41%
Power change[1]	12.13%	-0.73%	8.63%
My[1,3]	-17.48%	-23.02%	-10.27%
Mz[1,3]	-67.19%	-72.73%	-78.73

[1]Time average over one rotor revolution (six propeller revolutions)
[2]As a percent of the mean installed thrust
[3]As a percent of the mean installed torque

Table 4: Installation effect on propeller loads in hover

Figure 13 shows the installation effect on the contribution to thrust and power of one propeller blade along a full main rotor revolution (i.e. six propeller revolutions). First, it can be noted that there is almost no effect of the main rotor blade passage since the loads on the propeller is almost periodic. This could have actually been expected due to the very low level of RMS observed in the main rotor wake in isolated configuration. The change in blade thrust is almost sinusoidal and follow the expected behavior of an increase of thrust on the blade going up (rotor downwash is adding to the tangential velocity of the propeller blade) and a decreases on the blade going down. It reinforces the fact that the propeller behavior is mainly driven by the main rotor downwash.

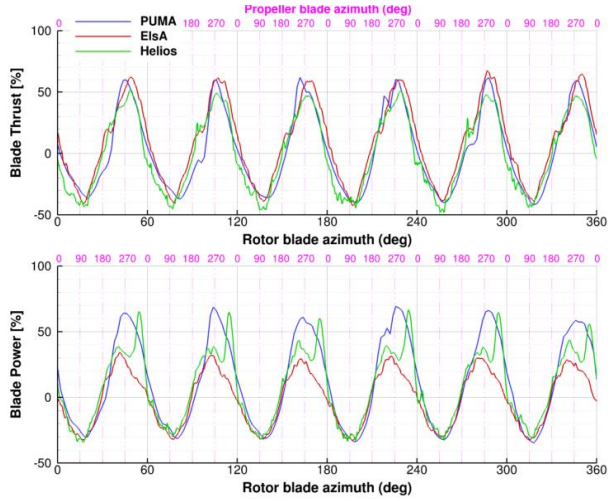

Figure 13: Installation effect on one propeller blade thrust and power in hover (one main rotor revolution)

The differences observed on the time-averaged values are due to the fact that in Helios the decrease of thrust on one half of the revolution is perfectly balanced by the increase on the other half, while for elsA the increase is slightly larger (+60%) than the decrease (-50%) leading to an 10% increase of time-averaged thrust. Overall, all the tools agree relatively well on the thrust fluctuations, whose amplitude (roughly +-50%) has to be kept in mind while designing propellers for such kind of rotorcraft. Concerning the power, elsA is showing an almost sinusoidal variation ranging from -30% to +30% (leading to almost no change in time-averaged power), but it is actually not the case for other tools. They all agree very well with each other on the first half of the propeller disc (blade going down). But on the second part, PUMA is predicting a much larger increase of power, up to 60%, probably reaching the limit of blade stall in 2D airfoil datas, which is not foreseen by CFD solver due to 3D effects not accounted for in PUMA. Helios features an even more complex shape. A first peak of power increase is reached almost at the same position as other tools (250° propeller blade azimuth), with almost the same level as elsA. But then while elsA shows a smooth decrease, Helios features a second peak near 330° propeller blade azimuth reaching the same level as PUMA maximum.

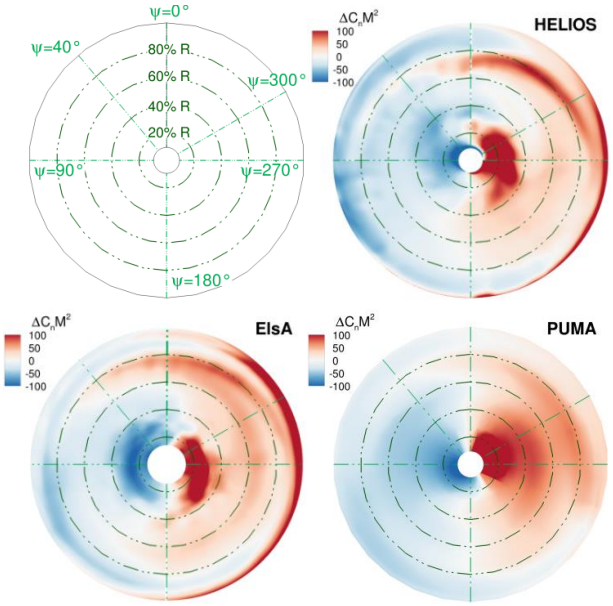

Figure 14:Change in propeller sectional load due to interactions in hover

The sectional loads (Figure 14) on the last propeller revolution confirm that all the tools give very similar results, with a decrease of lift on the blade down side and an increase on the other side of the disc, as already discussed. Most of the discrepancies are localized between 270° and 0°. Between these azimuths PUMA is showing a smooth evolution of the sectional lift over the entire blade span, while both CFD codes are featuring a peak at 80% radius roughly from 300° up to 40° azimuth. It is actually due to blade vortex interactions (Figure 15) which seem to be completely missed by the freewake approach, probably due to a coarse time step, blade discretization and large regularization parameters.

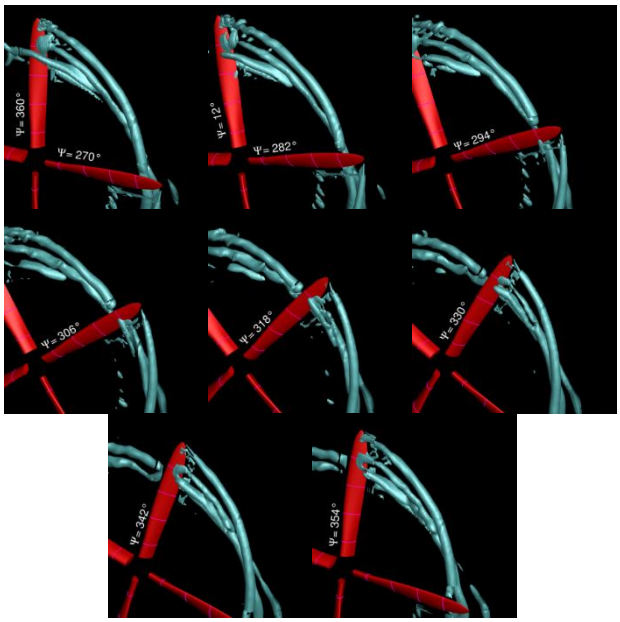

Figure 15. Visualization of blade vortex interactions between 270° and 360° propeller blade azimuth (elsA).

Figure 16 shows the spanwise distribution of blade loads normal to the sectional chord (CnM^2) and parallel to the chord (CcM^2) for propeller blade azimuth between 270° and 360°. Concerning the CnM^2, which mainly contribute to the thrust, both elsA and Helios are featuring a smooth decrease of loads over the blade span, leading to the formation of two peak in the loads at 360°, one at 95% radius and one around 70% radius. These two peaks are the footprint of the two previous blade tip vortex (Figure 15). While the peak values are roughly the same for both CFD computations, the decrease around 80% seems larger with Helios and could explain the slightly lower maximum value of thrust increase. Concerning the CcM^2, which mainly contributes to the torque and therefore the power, discrepancies between CFD codes are larger. Both agree on the fact that the drag is increasing at the tip from 270° to 300°. However, after 300° azimuth, in elsA, the drag starts to decrease smoothly, and the peak value decreases and spreads from 70% to 95% radius. On the other hand, using Helios, the peak value at 85% radius is decreasing rapidly and even goes below zero, but a second peak is appearing near 70% radius. This strong fluctuation between 60% and 95% radius is due to a complex interaction. As seen in Figure 15 the blade is interacting with two different tip vortices from previous blades which had interacted with each other sometimes before. Capturing such interactions is highly dependent on numerical parameters and CFD solvers. Moreover, the balance between these two peaks leads to the second peak of power increase seen around 330° propeller blade azimuth in Figure 13.

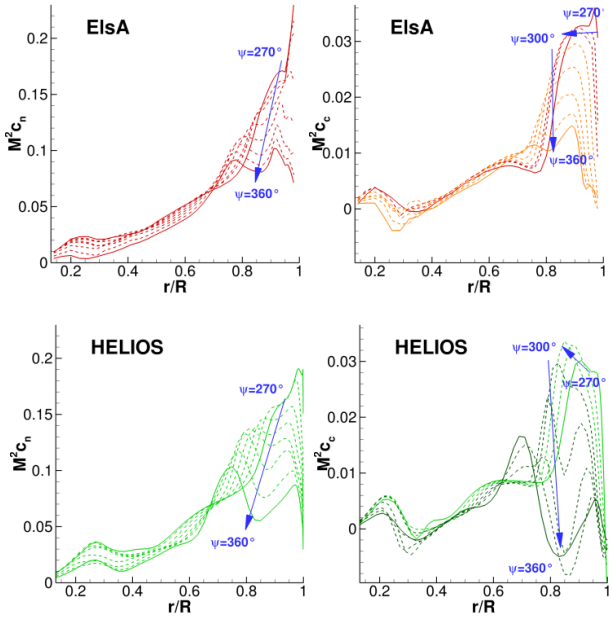

Figure 16. Spanwise distribution of blade loads normal to the sectional chord (C_nM^2) and parallel to the chord (C_cM^2)

As a conclusion, while the propeller aerodynamics is mainly driven by the main rotor downwash, the differences between numerical tools which could appear to be quite large on the integrated thrust and power (Table 4) are actually only due to their ability to capture BVI phenomenon that occurs locally on the propeller blades for azimuth between 270° and 360°. It is well known that numerical simulation of BVI is extremely sensitive to numerical scheme, and meshes. Helios seems to capture BVI with less dissipation leading to stronger interactions (Helios uses a 5th order scheme and a grid size in the Cartesian grid of 5% of propeller chord, while elsA uses a second order scheme with a grid size of 9% of the propeller blade chord.)

5.2. Low advance ratio (Mu=0.05)

At a low advance ratio, the propeller is no longer fully immersed in the main rotor wake. As seen in Figure 17, at μ=0.05, the main rotor wake impels only the upper part of the propeller disc and produces a smaller deviation of the propeller wake than in hover.

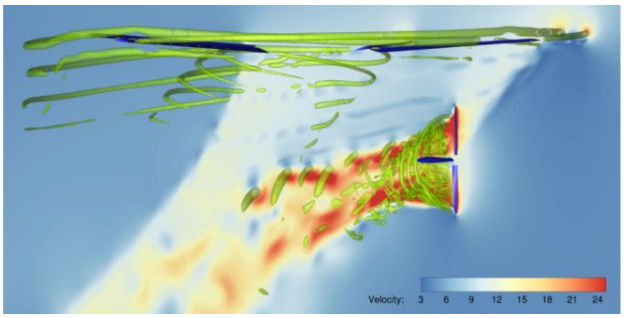

Figure 17. Velocity in a plane perpendicular to the propeller disc at μ=0.05

Presented at 47th European Rotorcraft Forum, United Kingdom, 7-9th September, 2021

Such conditions are still quite challenging for free wake approach and even if it is not as critical as in hover, the tuning of the numerical parameters in order to avoid divergence had been once again mandatory and therefore could affect the results.

5.2.1. Effect on the main rotor

Table 5 illustrates installation effects on the propeller forces and moments for the different numerical tools.
All computations seem to agree on an increase in time-averaged thrust and power on the main rotor. CFD codes show an increase of 1% on both thrust and power, while free wake computation overestimates both values: 2% on the thrust and 3% on the power.

	Thrust[1] [%]	Power[1] [%]
PUMA	2.07%	3.63%
elsA	0.94%	1.00%
Helios	1.34%	0.94%

[1]Time average over one rotor revolution (six propeller revolutions)

Table 5. Installation effect on main rotor thrust and power at advance ratio 0.05

However, it was already shown earlier that small effect on time-averaged loads does not mean no effect on the unsteady loads. Figure 18 shows the time history of the change in thrust and power on one rotor blade over one revolution. First thing to notice is that there are some high frequencies fluctuations on all the computations. Fluctuations frequency is higher with the CFD than with freewake and Helios shows larger amplitudes of the fluctuations.

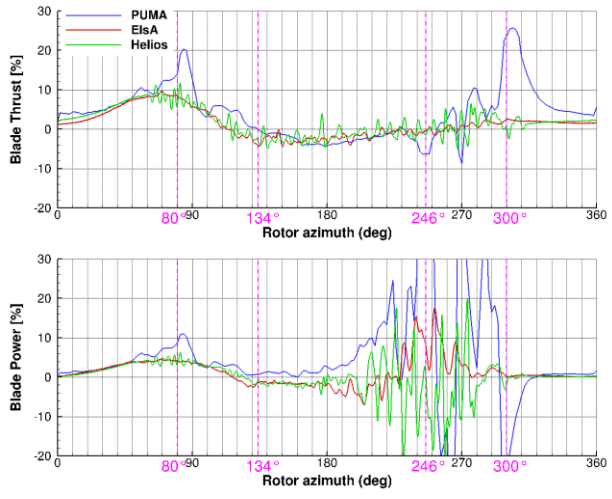

Figure 18. Installation effect on one main rotor blade thrust and power at an advance ratio of 0.05

When looking at the full rotor disc loads (Figure 19), we can see the same sort of high frequencies fluctuations located near the tip of the blade. Since on such high speed rotorcraft, the propulsive force comes from the propeller, there is no longer a need to tilt the rotorcraft in forward flight. Therefore, at advance ratio 0.05, blade vortex interactions on the main rotor are stronger than on conventional rotorcraft. When adding the propeller, the aerodynamics of the main rotor is changing, leading to slightly different blade tip vortex strength and path. The strong high frequency fluctuations seen in the figure are actually due to the fact that a percentage of loads changes is shown. The absolute values of the loads are actually smoother. PUMA is actually showing lower frequency changes due to the coarser time step and spanwise blade discretization used and the higher amplitude seen by Helios is due to its better capture of tip vortices (finer mesh and higher order numerical scheme lead to strengthen vortices).

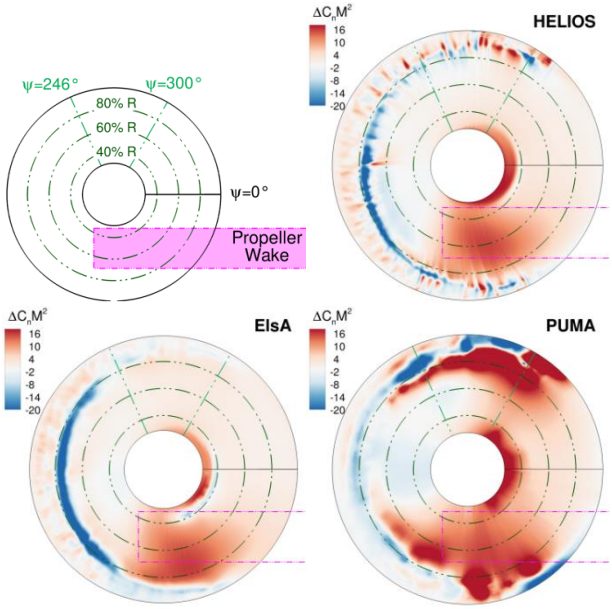

Figure 19. Change in main rotor sectional load due to interactions at advance ratio 0.05

What clearly differs from the hover case, at least on both CFD computations, is the changes on the retreating side. Even if the retreating side is largely affected by the high frequency fluctuations, some trends could be identified. The thrust is slightly affected by the propeller. Loss of thrust due to the propeller is visible up to 246° and then a small increase (below 2%) is shown. Only PUMA computation features a large peak of thrust near 300° azimuth. On the other hand, the power seems to be largely affected by the propeller on the retreating side. Large changes are seen between 180° and 300° for all codes along with extreme fluctuations. In Figure 19 it seems that those changes are once again mainly located near the tip.
Figure 20 shows the spanwise distribution of blade loads normal to the sectional chord (CnM^2) and parallel to the chord (CcM^2) for main rotor blade azimuth 246° and 300°, in installed configuration (plain line) and isolated configuration (dashed line). It can clearly be seen that the installation effect observed in CFD are only due to either a shift along the radius or a sharpening of the slope of the loads

near the tip, where blade vortex interactions are occurring. It confirms the fact that, on the retreating side, installation effects are essentially due to a change in the BVI behavior. In PUMA changes are affecting a larger part of the blade due to an over estimation of the vortex size from insufficient wake sheet roll up near the tip which is quite common for such approach.

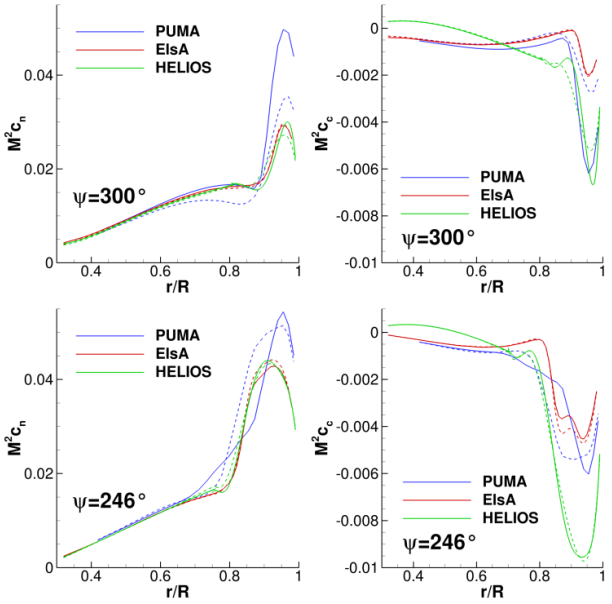

Figure 20. Spanwise distribution of rotor blade loads normal to the sectional chord (C_nM^2) and parallel to the chord (C_cM^2). (— installed, - - - isolated)

5.2.2. Propeller inflow characteristics

Figure 21 shows the three velocity component in the propeller plane from a computation of an isolated rotor. The line where each velocity is equal to zero is also shown. The line on which the difference between the freestream velocity and the local axial velocity is equal to zero can be seen as the edge of the main rotor wake.

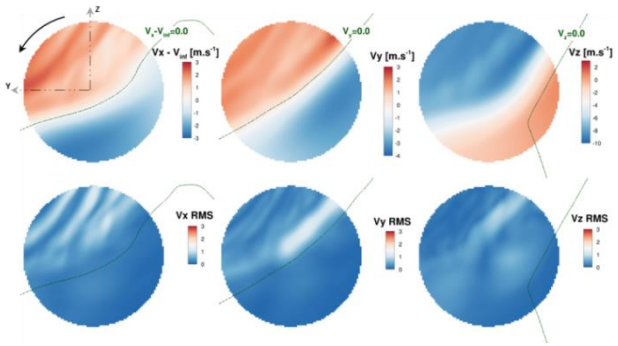

Figure 21. Velocity (mean value and RMS) in propeller plane from an isolated rotor computation (elsA) at advance ratio 0.05

As it was expected from Figure 17 it clearly appears that the main rotor propeller wake will impact the upper part of the propeller disc. In terms of axial velocity, the part of the propeller disc inside the rotor wake will encounter a small increase of axial velocity (2m.s^{-1}) while the part outside of the wake will see a decrease of approximately the same amount. The same observation can be made on the lateral velocity due to the swirl of the main rotor wake. Concerning the main rotor downwash, it introduces some large vertical velocity over most of the disc. Right inside the wake, it is of the order of 10m.s^{-1}, and it quickly decays outside of the wake. At last, as it was the case in hover, there are actually very few fluctuations of the flowfield in the vicinity of the propeller disc. The RMS remains below 1m.s^{-1} even on the edge of the main rotor wake. Accounting from this observations, we could expect that the propeller aerodynamics will be mainly dominated by the main rotor downwash, but, in this case, unevenly over the propeller azimuth.

5.2.3. Effect on propeller

Table 6 illustrates the installation effects on the time average propeller thrust and power for the different numerical tools over one rotor revolution (six propeller revolution). It also include the time average lateral (Fy) and vertical (Fz) forces (respectively moments) acting on the propeller in installed conditions as a percent of the thrust (respectively power). In isolated conditions these in plane forces and moments are strictly equal to zero. Concerning the thrust, while Helios and PUMA agree on roughly 5% loss of thrust, elsA is actually predicting a small gain of 1.6%. These discrepancies on the thrust are similar to the one observed in hover. However, all tools lead to similar amount of in plane loads, with almost no lateral force and a small vertical one, all of them lower than the one in hover. While the propeller is undergoing an important downwash on the upper part, the "averaged" downwash it seeing is lower than in hover.

	PUMA	*elsA*	HELIOS
Thrust change[1]	-5.40%	1.64%	-5.22%
Fy[1,2]	-0.55%	0.035%	-0.41%
Fz[1,2]	-2.85%	-3.8%	-2.06%
Power change[1]	-5.89%	-8.76%	-6.07%
My[1,3]	-10.22%	2.36%	-5.98%
Mz[1,3]	-26.02%	-14.16%	-26.41%

[1]Time average over one rotor revolution (six propeller revolutions)
[2]As a percent of the mean installed thrust
[3]As a percent of the mean installed torque

Table 6. Installation effect on propeller loads at advance ratio 0.05

Concerning the change in terms of power, consistency between the models is better. All of them are predicting a decrease of power ranging from 6% to 8%. However more discrepancies are found on the in plane moments which are non-negligible but again lower than in hover.
In order to better understand the reason for these differences we have to examine more local aerodynamic quantities. Figure 22 shows the

installation effect on the thrust and power of one propeller blade over a full main rotor revolution (i.e. six propeller revolutions). First of all, PUMA computation seems to suffer from a lack of convergence, since it is the only computation that does not reach a more or less periodic state over the propeller revolutions. However, for the last propeller revolutions, it reached similar trends as the CFD tools with even a very close agreement with Helios on the last one.

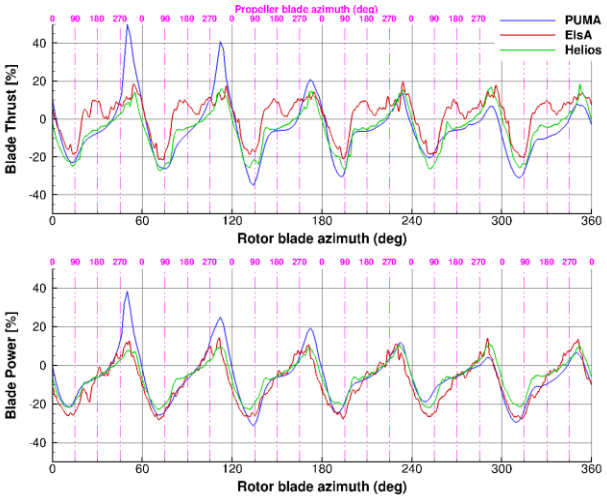

Figure 22. Installation effect on one propeller blade thrust and power over one rotor revolution at an advance ratio of 0.05

Both Helios and elsA have very similar levels of thrust and power change from 270° to 90° azimuth which is the area of the propeller immersed in the main rotor wake. The behavior is the one already described earlier: a somewhat sinusoidal shape of thrust change with an increase when the blade is going up (the downwash is added to the propeller blade tangential velocity, resulting in an increase of dynamic pressure) and a loss when the blade is going down (the downwash decreases the propeller tangential velocity).

However, when the blade is not inside the main rotor wake, behavior between elsA and Helios are more different, at least on the thrust. ElsA is showing a small but almost constant gain of thrust from 90° to 270°, while Helios is predicting a small but also almost constant loss of thrust. For this range of azimuth, Helios is somehow predicting trends similar to what is observed using PUMA. On the last propeller revolution PUMA and Helios are actually fitting very well.

Figure 23 shows the sectional loads change on the propeller blade due to the interactions during the last propeller revolution. The line for which the axial velocity is equal to the freestream one in the isolated main rotor computation is also shown in order to give an idea of the limit of the main rotor wake impact. It outlines the fact that inside the rotor wake, the blade going up shows an increase of loads over the whole span, and a decrease when it goes down. However, the fact that the main rotor wake is not at the exact same position with the three solvers leads to some differences in the azimuthal loads. This good correlation between the three solvers inside the main rotor wake is confirmed in Figure 24 for propeller blade azimuth 0°, 90° and 320°. Differences in Figure 22 and Figure 23 are actually mainly inherited from the isolated propeller loads, since installed loads are very similar at 0° and 90°. Moreover, inside the rotor wake in Figure 24 between 310° and 0° azimuth, elsA features some strong load increase near the tip. When looking at Figure 24 for azimuth 320°, it can be seen that, in Helios and elsA the increase is of the same order around 90% radius, differences only occur at the very tip of the blade where the load is going down in isolated case for elsA and not in Helios, outlining some tip vortex interaction effects as in hover case.

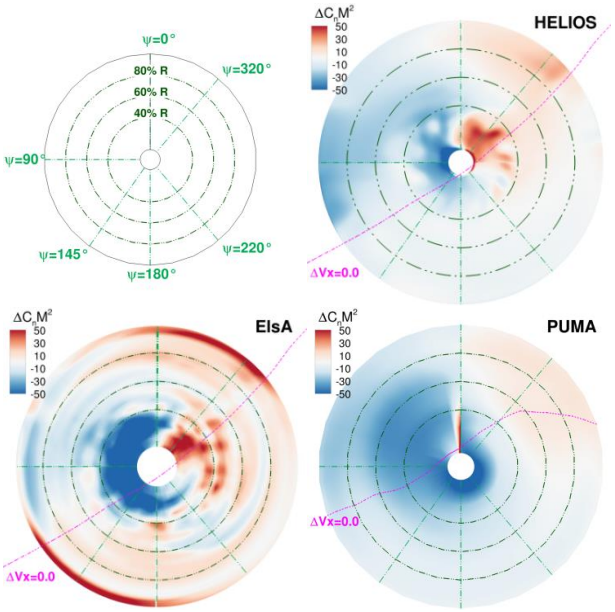

Figure 23. Change in propeller sectional load due to interactions at advance ratio 0.05

Concerning the effect on the loads while the blade is out of the main rotor wake, Figure 23 confirms what was seen in Figure 23, PUMA and Helios seem to be in good agreement, and elsA is featuring more discrepancies. In Figure 25, for propeller blade azimuth 145°, 180° and 220° Helios shows almost no differences in the loads over the whole span of the blade. ElsA shows some oscillations in the load over the span, both in isolated computation and installed one. The increase of loads in installed configuration from elsA is not evenly spread over the span and is due either to the disappearing or to the change in radial position of these fluctuations between isolated and installed case. The origin of these fluctuations in isolated computation has yet to be determined. The overall very small effects on the loads outside of the main rotor wake confirm that the effect on the propeller loads is mainly driven by the main rotor downwash, which rapidly drops to zero out of the

wake. In this area the small effect seen is a combination between the change in axial and lateral inflow velocity, which is of the order of less than 2 $m.s^{-1}$. Such amount will not lead to significant change in terms of velocity nor angle of attack at the blade section due to the high RPM of the propeller.

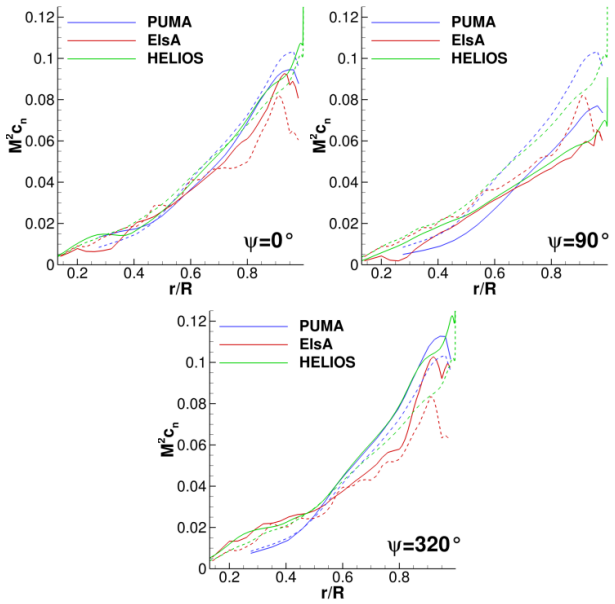

Figure 24. Propeller sectional load radial distribution at advance ratio 0.05 for azimuth 0°, 90° and 320° (— installed, - - - isolated)

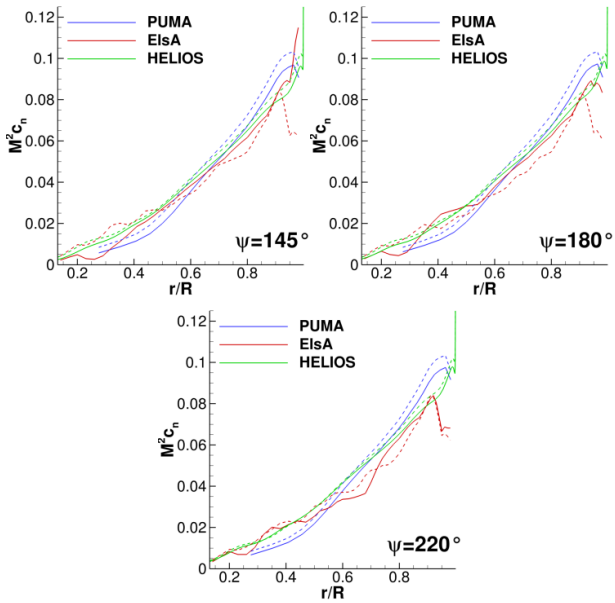

Figure 25. Propeller sectional load radial distribution at advance ratio 0.05 for azimuth 145°, 180° and 220° (— installed, - - - isolated)

6. CONCLUSIONS

In this study, rotor / propeller wake interactions were analyzed for a given propeller position at different advance ratios and using three different solvers. The previous computations from [7] were improved and compared with another CFD solver leading to a better understanding of the phenomena involved. Only two cases were analyzed here since the conclusions for the third one (high advance ratio) drawn in [7] were confirmed with the second CFD solver.

6.1. Effect on the main rotor

All the computations agree on the fact that the main rotor is only slightly affected by the propeller in terms of time-averaged loads. However, when the blade is moving over the propeller wake, sectional loads increase due to the blockage effect of the propeller wake. On the part of the disc in front of the propeller, the loads are lowered due to the suction effect of the propeller. Effects on the retreating side results from small differences in the root and tip vortices strengths and path. These trends are amplified at low advance ratio compared to the hover case.

6.2. Effect on the propeller

In hover and at low advance ratio (μ=0.05), the propeller aerodynamic behavior is mainly driven by the main rotor downwash.

In hover, all solvers predict some extreme fluctuations of loads (up to 50%) in an almost sinusoidal way, not depending on the main rotor blade passage, along with important in plane forces and moments. Propeller is also encountering some blade vortex interactions on the upper part of the disc leading to discrepancies between solvers due to their different capability to capture this phenomenon. Moreover this BVI could be of importance in noise signature.

At the low advance ratio, the fluctuations are lower and mainly located on the part of the propeller inside the main rotor wake. Outside of the wake, effects of the main rotor on the propeller are quite small.

In any case, the propeller is also undergoing some important in plane loads and moments which have to be taken into account in the design of such rotorcraft.

6.3. Numerical modeling

Overall, all CFD solvers capture the same aerodynamic phenomenon. The free wake approach suffers from important numerical instabilities, but still provides some good insight of the aerodynamics of the propellers at a much lower cost than CFD. However, the precise aerodynamics of the main rotor, is out of reach for such approach.

At last, it should be kept in mind that the computations were performed at the prescribed trim from an isolated computation, while on a real rotorcraft the flap and lead-lag motion of the blade may be largely affected by the fluctuations of loads changing the interactions and also introducing some vibrations. Moreover, only one propeller was modeled and no rotor head and fuselage were used. Modeling a full rotorcraft will likely increase the complexity of the interactions.

Presented at 47th European Rotorcraft Forum, United Kingdom, 7-9th September, 2021

7. ACKNOWLEDGMENTS

Part of this work was granted access to the HPC resources of CINES under the allocation 2017-A0032A10264 made by GENCI.
Part of the material presented in this paper is a product of the HPCMP CREATE™-AV Element of the Computational Research and Engineering for Acquisition Tools and Environments (CREATE) Program sponsored by the U.S. Department of Defense HPC Modernization Program Office.
This paper is the result of a multi-year collaborative research under the US/French Project Agreement for Helicopter Aeromechanics, involving US Army CCDC AvMC and Georgia Institute of Technology (GIT) on the US side and ONERA (the French Aerospace Lab) on the French side.
The author also acknowledges APC propellers for providing the geometrical description of the propeller blades.

8. REFERENCES

[1] A. Le Pape, J. Gatard, J-C. Monnier: “Experimental Investigations of Rotor-Fuselage Aerodynamic Interactions Using a Helicopter Powered Model”, 30th European Rotorcraft Forum, Marseille, France, 14-16 September, 2004
[2] B.G. van der Wall, A. Bauknecht, S.N. Jung, Y.H. You: “Semi-Empirical Physics-Based Modeling of Fuselage-Rotor and Fuselage-Wake Interferences for Comprehensive Codes”, 70th Annual Forum of the American Helicopter Society, Montreal, Canada, May 20-22, 2014
[3] G.N. Barakos,R. Steijl, M. Woodgate, “CFD for Rotorcraft Recent Progress and new Challenges with the GoAhead case”, 29th Congress of the International Council of the Aeronautical Sciences, St Petersburg, Russia, 8-11 September, 2014
[4] M. Ramasamy: “Measurements Comparing Hover Performance of Single, Coaxial, Tandem, and Tilt-Rotor Configurations”, 71th Annual Forum of the American Helicopter Society, Phoenix, USA, May 20-22, 2013
[5] Bain, L. J., Landgrebe, A. J., "Investigation of Compound Helicopter Aerodynamic Interference Effects", USAAVLABS Technical Report 67-44, November 1967
[6] P. Bowles et al. "A Model-Scale Wind-Tunnel Study of Main Rotor/Propeller Interference", 72nd AHS annual forum, West Palm Beach, Florida, May 17-19, 2016
[7] R. Boisard "Aerodynamic investigation of rotor / propeller interactions on a fast rotorcraft", 44th European rotorcraft forum, Delft, Netherland, September 18-21, 2018.
[8] A. Le Pape, J. Gatard, J-C. Monnier, "Experimental Investigations of Rotor-Fuselage Aerodynamic Interactions." Journal of the American Helicopter Society 52.2 (2007) 99-109.
[9] https://www.apcprop.com/
[10] Mudry, M., "La théorie des nappes tourbillonnaires et ses applications à l'aérodynamique instationnaire", Thèse de Doctorat d'état, Université Paris VI, July 1982
[11] Q. Gallas, R. Boisard, J.-C. Monnier, J. Pruvost, A. Giliot, "Experimental and numerical investigation of the aerodynamic interactions between a hovering helicopter and surrounding obstacles", 43nd European rotorcraft Forum, Milan, Italy, 12-14 September, 2017
[12] R. Boisard, "Aerodynamic investigation of a helicopter rotor hovering in the vicinity of a building", 74th AHS forum, Phoenix, Arizona, USA, 14-17 May 2018.
[13] L. Cambier, S. Heib, S. Plot, “The Onera elsA CFD software: input from research and feedback from industry,” Mechanics & Industry, 14, pp 159-174, 2013
[14] I. Mary, P. Sagaut, M. Deville (2000). "An algorithm for unsteady viscous flows at all speeds". In: International Journal for Numerical Methods in Fluids 34, pp. 371–401
[15] J.C. Kok, "Resolving the Dependence on Freestream Values for the k- Turbulence Model", AIAA Journal 38.7 (2000), p. 1292–1295.
[16] Wissink, A. M., Sitaraman, J., Jayaraman B., Beatrice, R., Lakshminarayan, V. K., Potsdam M., Jain R., Bauer, A., and Strawn, R., “Recent Advancements in the Helios Rotorcraft Simulation Code,” AIAA 2016-0563, 54th AIAA Aerospace Sciences Meeting, AIAA SciTech Forum, San Diego, California, January 4-8 2016.